Microstructural characterization and validation of a 3D printed phantom for diffusion MRI

Farah N. Mushtaha[1,†] , Tristan K. Kuehn[1,3,†], Omar El-Deeb[6], Seyed A. Rohani[3], Luke W. Helpard[3], John Moore[5], Hanif Ladak[2,3,7], Amanda Moehring[6], Corey A. Baron[1,2,3,4,5,‡] , Ali R. Khan[1,2,3,4,5,‡]

[1] *Centre for Functional and Metabolic Mapping, Robarts Research Institute, Western University, London, Canada*

[2] *Department of Medical Biophysics, Schulich School of Medicine and Dentistry, Western University, London, Canada*

[3] *School of Biomedical Engineering, Western University, London, Canada*

[4] *The Brain and Mind Institute, Western University, London, Canada*

[5] *Imaging Research Laboratories, Robarts Research Institute, Western University, London, Canada*

[6] *Department of Biology, Western University, London, Canada*

[7] *Department of Electrical and Computer Engineering, Western University, London, Canada*

† Farah N. Mushtaha and Tristan K. Kuehn are co-first authors

‡ Ali R. Khan and Corey A. Baron are co-senior authors

Abstract

Purpose

To introduce and characterize inexpensive and easily produced 3D-printed axon-mimetic (3AM) diffusion MRI (dMRI) phantoms in terms of pore geometry and diffusion kurtosis imaging (DKI) metrics.

Methods

Phantoms were 3D-printed with a composite printing material that exhibits microscopic fibrous pores. Confocal microscopy and synchrotron phase contrast micro-CT imaging were performed to visualize and assess the pore sizes. dMRI scans of four identical phantoms and phantoms with varying print parameters were performed at 9.4T. DKI was fit to both datasets and used to assess the reproducibility between phantoms and effects of print parameters on DKI metrics. Identical scans were performed 25 and 76 days later to test their stability.

Results

Pore segmentation showed 33.6% of pores with diameters of 1.5-8μm with mean, median, and standard deviation of 20μm, 13μm, and 20μm, respectively. Phantoms with identical parameters showed a low coefficient of variation (~10%) in DKI metrics. Printing temperature and speed had a small effect on DKI metrics (<16%) while infill density had a larger and more variable effect (>16%). The stability analysis showed small changes over 2.5 months (<7%).

Conclusion

3AM phantoms can mimic the fibrous structure of axon bundles on a microscopic scale, serving as complex, anisotropic dMRI phantoms.

Keywords

Diffusion MRI, Validation, Modeling and Analysis.

1. Introduction

Diffusion magnetic resonance imaging (dMRI) produces images by sensitizing the MRI signal to the random motion of water molecules on a micrometre scale. This sensitivity means that dMRI signal reflects patterns of water diffusion in the brain imposed by brain microstructure. To ease the interpretation of dMRI signal, signal representations like

diffusion kurtosis imaging (DKI) (1) have been developed. By fitting raw dMRI data to mathematical representations whose parameters describe general features of the underlying diffusion, this technique produces metrics that are related to the microstructure and structural connectivity of the brain (1). However, a limitation of this approach to characterizing brain microstructure is that there is typically no *in-vivo* ground truth to validate the findings of a given study.

A number of techniques have been used to produce data for the validation of dMRI models, including numerical phantoms (2,3), *ex-vivo* brain samples (4,5), *in-vivo* studies (6), and physical phantoms (7,8). Numerical phantoms are simulations of diffusion behaviour under explicitly defined conditions and geometries. They allow precise experimental control, but do not reproduce all the complexity inherent to a real scan. *Ex-vivo* studies are performed by imaging animal brains *in vivo*, then sacrificing animals and analysing histological sections of the animals' brains to validate the findings of the imaging study (9). These methods provide data directly from a real brain, but histology is a time-consuming and costly approach that covers a limited region of interest in the brain that is difficult to register to a dMRI scan. Further, there may be microstructural changes in the tissue due to histological preparation/fixation. Physical phantoms are artificial objects designed to mimic the diffusion characteristics of the brain, producing dMRI scan data similar to that seen from real brains. Physical phantoms occupy a middle ground between the two ends of a spectrum defined by numerical and *ex-vivo* studies: they produce real scan data with a well-known microstructural ground truth, but are not as customizable as numerical phantoms or as true to the structure of the brain as *ex-vivo* samples.

Several types of physical phantoms have been previously proposed. Glass capillaries (10) provide reliably anisotropic diffusion in a pattern that is straightforward to characterize, but cannot mimic some complex geometric fibre configurations that are observed in the brain. Straight fibres can be produced with axon-scale diameters to mimic hindered diffusion between axons, but are difficult to arrange with the geometric complexity of some brain regions. Extruded or electrospun hollow fibers (11) mimic axonal diffusion patterns well, but are expensive and time-consuming to produce. As such, the development of dMRI phantoms involves trade-offs between the cost of materials and equipment, ease of production, the ability to achieve accurate brain-mimetic microstructure, and geometric complexity. Using existing procedures to produce a physical phantom with biologically plausible microstructure

and geometric complexity is expensive and time-consuming, so an alternative that is both adequately brain-mimetic and easy to produce is needed.

Fused Deposition Modeling (FDM) 3D printing is an inexpensive and flexible manufacturing technique that enables repeatable production of custom parts. FDM works by melting a polymeric filament and depositing the molten material one line at a time in a sequence of layers. FDM can control the physical properties of printed objects by changing parameters like the temperature of the print head and speed at which material is deposed. It also allows the within-layer print path to be designed to adjust the overall material properties of the finished product. Given the flexibility and low cost of FDM, it would be advantageous to apply it to the production of physical dMRI phantoms.

For the FDM production of 3D-printed Axon Mimetic (3AM) phantoms, we propose the use of a dual component “porous filament” material (12). In this work, we utilized “GEL-LAY” (LAY Filaments, Cologne, Germany), which is composed of an elastomeric matrix infused with pockets of polyvinyl alcohol (PVA). When 3D printed, the PVA forms long fibres within each line of printed composite material. PVA is water-soluble, so when this 3D printed material is immersed in water, the PVA fibres dissolve, leaving behind microscopic fibrous pores, as illustrated in Figure 1a. The anisotropic structure of these fibrous pores mimic the anisotropic shape of axonal fibres and restrict diffusion in a similar way, allowing 3D printed porous filaments to form the basis of a phantom that can validate dMRI (13).

For 3AM phantoms to be useful, their pores’ size should be as close as possible to axon diameters seen in the human brain, which are typically on the order of 1-5 μm. Furthermore, the pores’ orientations must be well-known and should be controllable. The overall T_1 and T_2 relaxation times modulate the achievable SNR in a scan of the phantoms (14), so phantom materials should shorten relaxation times as little as possible. A dMRI scan of a 3AM phantom should show diffusion characteristics as similar to those seen in the human white matter as possible. Any dependence of those diffusion characteristics on 3D print parameters should be identified to facilitate customization of individual phantoms. Finally, 3AM phantoms’ diffusion characteristics should be consistent from print to print and should be as stable as possible over time.

In this study, we use both fluorescent microscopy and synchrotron phase-contrast micro-computed tomography, a novel technique that allows exceptionally fine-resolution 3D

visualization of soft structures, to characterize and visualize the microstructure of 3AM phantoms, assessing their suitability for use as axon-mimetic dMRI phantoms. We examine the effects of FDM printing parameters on dMRI acquired in the phantoms, and assess the reproducibility and stability over time of 3AM phantoms' dMRI characteristics.

2 Materials and Methods

2.1 Phantom preparation

An open protocol for producing 3AM phantoms has been developed and released as part of an Open Science Framework project (available in the Supplementary Materials and hosted at osf.io/zrsp6). Required materials include an FDM 3D printer, a dual component "porous filament" material, a vacuum chamber, and a set of watertight containers. The protocol was used to produce all phantoms for this study.

All phantoms were designed using the open-source Ultimaker Cura software, and were printed with an Ultimaker 3 Extended 3D printer (Ultimaker, Geldermalsen, The Netherlands) loaded with GEL-LAY filament. Unless otherwise noted, phantoms were printed with printing parameters recommended by the material vendor (Table 1), and the same pattern of parallel lines of material in each layer.

After printing, phantoms to undergo dMRI scanning were immersed in 1L of room temperature water (~23 °C) for 168 hours, then 20 mL of surfactant was added to decrease surface tension and allow the water to more easily enter the pores. The container was placed in a vacuum chamber at 1 bar for 48 hours to remove air bubbles. Finally, the phantoms were stacked in a test tube with distilled water for imaging (Figure 1b-d).

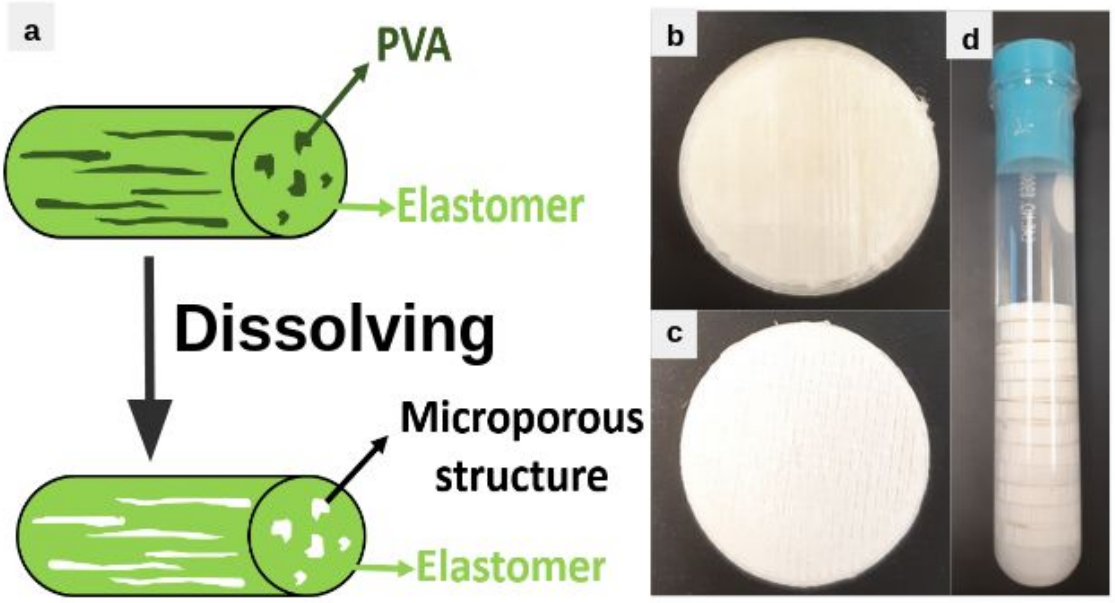

Figure 1. a) PVA dissolves away when placed in water leaving microporous structure. b) 3AM phantom before dissolving. c) 3AM phantom after dissolving. d) Dissolved 3AM phantoms stacked in a test tube with water that are ready for imaging.

2.2 Microscopy

Three block-shaped 3AM phantoms with dimensions 25 mm × 15 mm × 35 mm were printed with vendor-recommended printing parameters. The blocks were immersed in water for 18 hours to soften by allowing a small portion of the PVA to dissolve. Afterwards, the blocks were sliced into 50 μm slices using a Shandon Finesse ME+ microtome (ThermoScientific). The slices were immersed in deionized water for 3 hours to allow the remaining PVA to fully dissolve. They were then immersed in diluted Rhodamine Beta (Rhodamine B) and placed in a vacuum chamber at 1 bar for 20 minutes to infuse the dye into the slices and eliminate air bubbles. The slices were then mounted on positive microscope slides.

Confocal microscopy was performed to obtain high resolution images using a Leica SP5 laser system microscope with a 40X oil-immersion objective lens. Z-stacks of phantom slices were acquired using 1.0 μm step size for axial ranges between 5-17 μm. To qualitatively visualize the pores in each sample, every z-stack was either averaged across all slices to produce a 2D image or rendered into 3D volumes using Leica Las X.

Using MATLAB's image processing toolbox, an averaged z-stack confocal microscopy image was converted to grayscale, then an adaptive thresholding technique (15) was used to compute an initial segmentation of the image. The initial segmentation was opened with a disc-shaped structuring element of radius 1 pixel to eliminate pixels spuriously identified as containing material. The resulting segmentation was then morphologically closed using a disc-shaped structuring element of radius 8 pixels to eliminate small regions spuriously identified as pores. Finally, the equivalent radius of each region identified as a pore was calculated.

2.3 Synchrotron phase contrast micro-CT

A cylindrical phantom with a diameter of 5 mm and height of 4.5 mm was 3D printed, immersed in water for two days, and allowed to dry. A propagation-based phase-contrast micro-computed tomography (micro-CT) scan was then performed in air at the Biomedical Imaging and Therapy beamline (05ID-2) at the Canadian Light Source Inc. (Saskatoon, Canada), using an energy of 30 keV, 3000 projections over 180°, 150 ms exposure time and 700 ms time per projection, total scan time of 1 hour, FOV=4096 × 4096 × 3456 μm^3 (L × W × H), and an effective isotropic pixel size of 1.65 μm.

2.4 MRI scanning and model fitting

Phantoms to undergo dMRI scanning were all scanned with the same parameters. Diffusion MRI was implemented with a 9.4 T Bruker small animal scanner using: 120, 60 and 20 directions at b=2000, 1000, and 0 s/mm^2, respectively, TE/TR=37/2500 ms, FOV=200×200 mm^2, 0.7 mm isotropic in-plane resolution, and one 3 mm axial slice per phantom.

For every resulting diffusion-weighted image, DiPy (16) was used to compute diffusion kurtosis imaging (DKI) metrics at each voxel.

A T1-mapping rapid acquisition relaxation enhancement (RARE) scan and a T2-mapping multi-slice-multi-echo (MSME) scan were performed on a set of eight phantoms with different 3D print parameters (Section 2.6). Both scans were implemented with a 9.4 T Bruker small animal scanner, FOV=40×40 mm^2, 0.3125 mm isotropic in-plane resolution, and one 3 mm axial slice per phantom. The T2 mapping scan was performed with 16 echoes having TE ranging from 6.5 to 104 ms and TR=2000 ms. The T1 mapping scan was performed with TE

= 5.7 ms, TRs of 500, 1000, 1500, 2000, and 3000 ms, and ETL = 2. To assess typical T1 and T2 values in 3AM phantoms, the mean and standard deviation T1 and T2 were calculated in the phantom produced with the nominal print parameters recommended by the manufacturer.

2.5 Phantoms for assessing the reproducibility of dMRI metrics

Four identical cylindrical 3AM phantoms were prepared with nominal printing parameters following the procedure outlined in Section 2.1. The phantoms were scanned with four axial slices and a scan time of 8.5 min, and DKI was fit to the scan data, all according to the imaging protocol outlined in Section 2.4. The coefficient of variation across all voxels in the phantoms was calculated for each DKI metric to assess the consistency of each metric across phantoms produced under identical conditions.

2.6 Phantoms for assessing stability over time and the effect of print parameters on dMRI

Eight cylindrical 3AM phantoms were produced according to the 3AM phantom protocol outlined in section 2.1, each with a width of 22 mm and height of 4.4 mm, composed of 44 layers of parallel lines.

Four FDM print parameters were altered across different phantoms to test their effects on the 3AM phantom's microstructure. The four altered parameters include the temperature at which the phantoms are printed, the speed of printhead travel during the 3D print, the thickness of each layer printed in the phantom, and the infill density, which refers to the proportion of each layer taken up by material, and is altered by changing the distance between adjacent lines of material within each layer. One phantom was printed with the nominal print parameters recommended by the substrate manufacturer, and for each parameter, one phantom was printed with that parameter lower than nominal, and one phantom with that parameter higher than nominal (where applicable), as summarized in Table 1.

The eight phantoms were scanned with four axial slices and a scan time of 8.5 min per each of two dMRI scans to cover the test tube and DKI was fit to the data, all according to the

protocol outlined in Section 2.5. The variation in each DKI metric was then assessed across the phantoms with each difference in print parameter.

To investigate the phantoms' stability over longer time periods, identical dMRI scans and model fitting procedures were performed 25 and 76 days later, and the variations in each DKI metric in the phantom produced with nominal parameters across time was assessed.

Table 1. The parameters used to print the phantoms.

Printing parameter	Low setting	Nominal setting	High setting
Printing temperature (°C)	215	225	235
Printing speed (mm/s)	20	30	50
Layer thickness (mm)	0.06	0.1	0.14
Infill density (%)	75	100	-

3. Results

3.1 Microscopy

Confocal microscopy images revealed two types of pores present in the phantoms: larger pores (70-150 μm in diameter) that are believed to have been created by material tearing during the microscopy preparation process and gaps being left between lines of material (Figure 2), and smaller pores (1-30 μm in diameter) created by the dissolving of PVA fibres (Figure 3). The images also clearly showed the larger-scale arrangement of each line of material deposited during the 3D printed process.

Segmentation of individual pores showed that most pores in the microscopy sample had a cross-sectional diameter between 1.5-8 μm with a mean of 20 μm, a median of 13 μm, and a standard deviation of 20 μm (Figure 3).

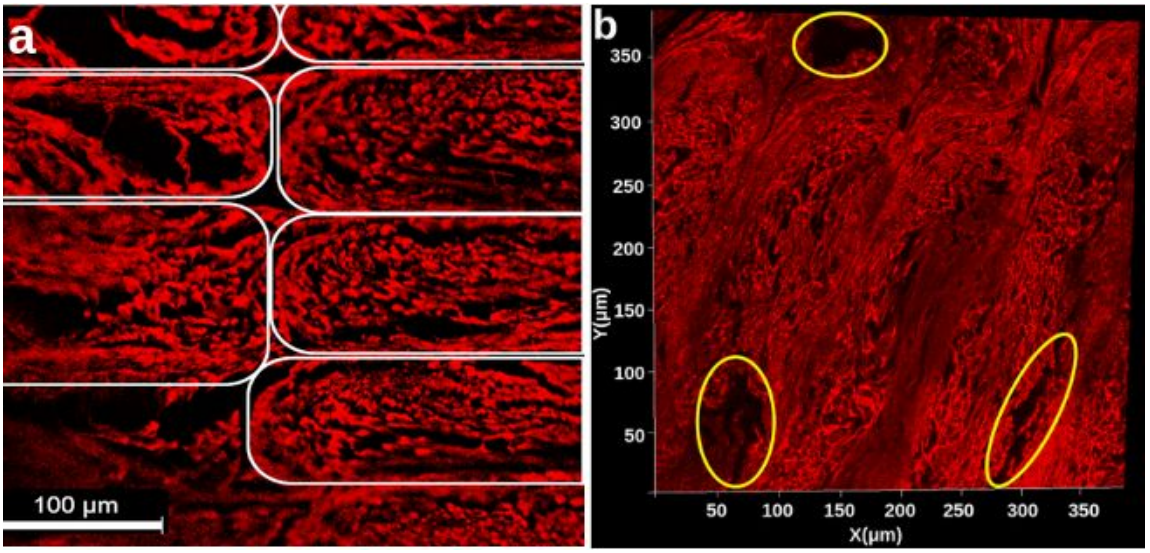

Figure 2. a) Confocal microscopy z-stack image of a stained cross sectional phantom sample, averaged across slices. Elastomeric matrix (red) and pores (black) are visible. The white outline indicates individual lines of material. b) 2D projection of a 3D microscopy volume acquired with confocal microscopy. Regions shown in red are the matrix of the 3AM phantom that is composed of elastomer while the black regions are pores. Outlined in yellow are larger pores caused by the printing pattern of the phantom. In both a and b, the image plane is perpendicular to the long axis of the pores.

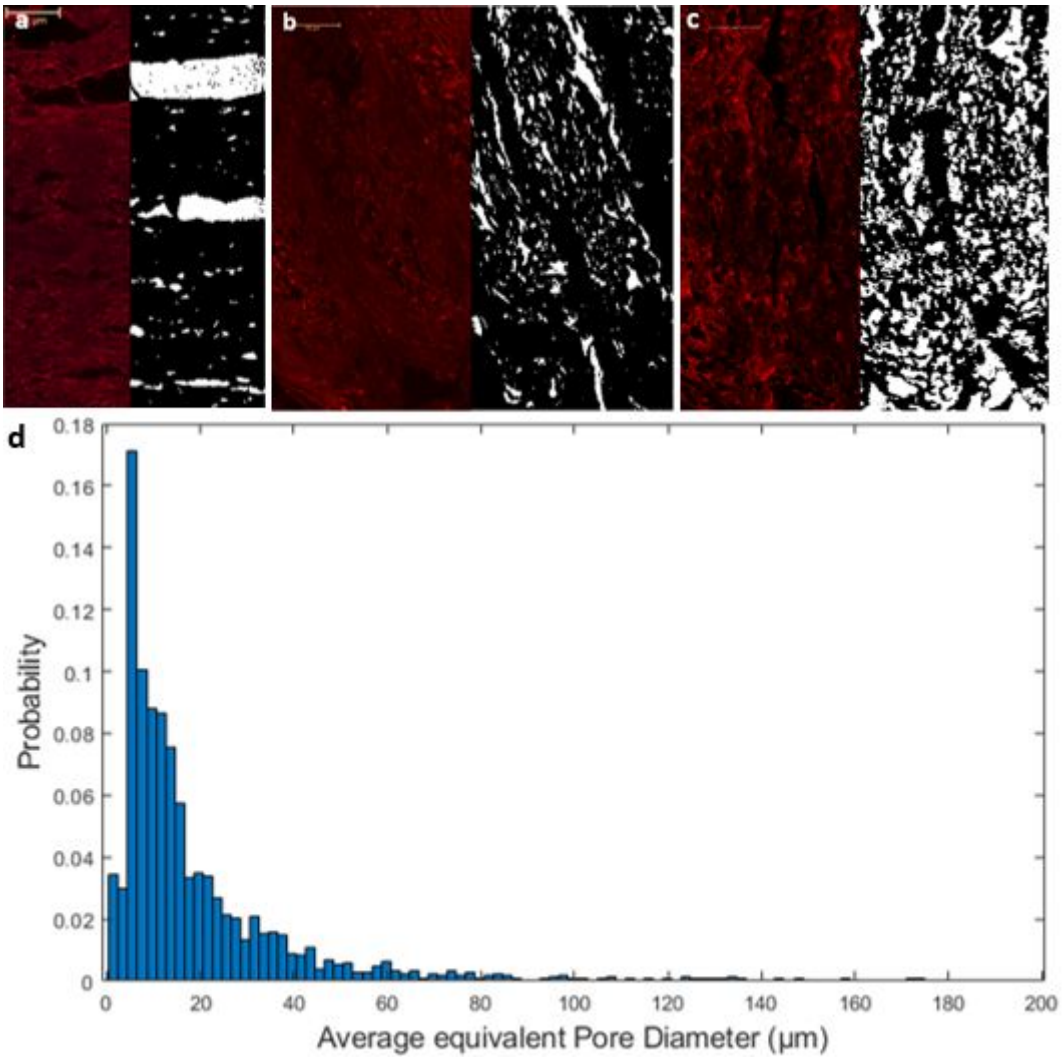

Figure 3. Pictures a-c, Confocal microscopy image before (left) and after (right) performing pore segmentation. d) normalized histogram of equivalent diameter of pores obtained from segmentations in a-c and their frequencies (Total N = 1912).

3.2 Micro-CT

The propagation-based phase-contrast micro-CT image showed anisotropic pores that run parallel to the primary travel direction of the 3D print head (Figure 4), supporting the findings of the confocal microscopy. These pores had typical diameters on the order of ten microns and typical lengths in the hundreds of microns.

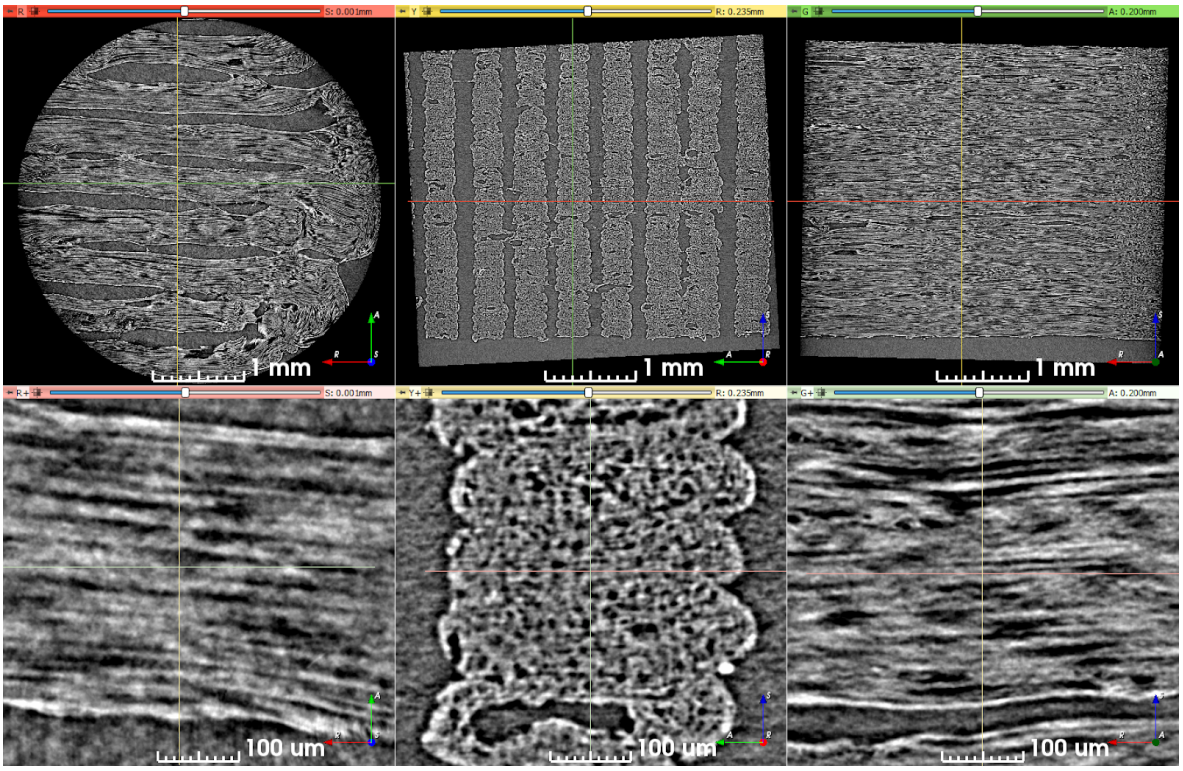

Figure 4. Synchrotron micro-CT scan data at two zoom levels, transformed to align lines of material with the viewing planes. Upper row: View of the entire scan ROI. Lower row: Detailed view of a short length of five stacked lines of material. The direction of print-head motion was left-right in the left- and right-most columns, and perpendicular to the image in the center column.

3.3 Nominal phantom characteristics and reproducibility

The mean T1 and T2 measured in a phantom printed with nominal printing parameters were 3960 ± 425 ms and 119 ± 21 ms, respectively.

The mean dMRI characteristics across all voxels of the 4 nominal phantoms are summarized in Table 2. The axial diffusivity (AD) is close to the diffusivity of pure water at room temperature (0.0022 mm^2/s), and the radial diffusivity (RD) is about half the AD. The axial kurtosis (AK) is close to zero, and the lack of kurtosis in the axial direction is supported by a near-linear relationship between ln(S) and b from acquisitions with diffusion encoding direction close to the axial direction (Figure 5).

The coefficient of variation (%) for each DKI metric across 4 identical nominal phantoms was calculated as a measure of repeatability. The highest coefficient of variation reported was 13.2% for RD, and the rest were lower than 10.5%.

Table 2. Mean dMRI metrics from 4 nominal phantoms and their coefficient of variation.

Metric	Mean Value	Standard Deviation	Coefficient of variation (%)
AD ($\times 10^{-3}$ mm^2/s)	2.13	0.05	3.19
RD ($\times 10^{-3}$ mm^2/s)	1.01	0.08	13.20
MD ($\times 10^{-3}$ mm^2/s)	1.38	0.07	8.78
FA	0.46	0.03	5.24
AK	0.07	0.01	10.10
RK	1.13	0.07	6.31
MK	0.52	0.02	1.86

Note: axial kurtosis, AK; radial kurtosis, RD; Mean kurtosis, MK; axial diffusivity, AD; radial diffusivity, RD; Mean diffusivity, MD; fractional anisotropy, FA.

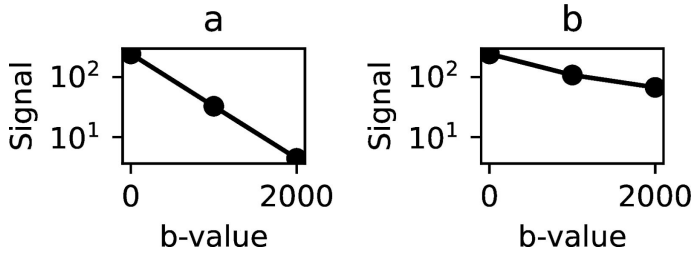

Figure 5. Expected signal vs. b-value from the DKI fit in a) the axial direction, and b) the radial directions.

3.4 Metric variation with print parameters

Changes in the mean value of each metric with every print parameter were small for every print parameter except infill density (Figure 6). Excluding infill density, the difference from the nominal case was less than 16% for all metrics except AK, which had very high percent

differences in some cases due to mean values close to zero. An increase in infill density of the phantom resulted in an increase in fractional anisotropy and a decrease in radial diffusivity.

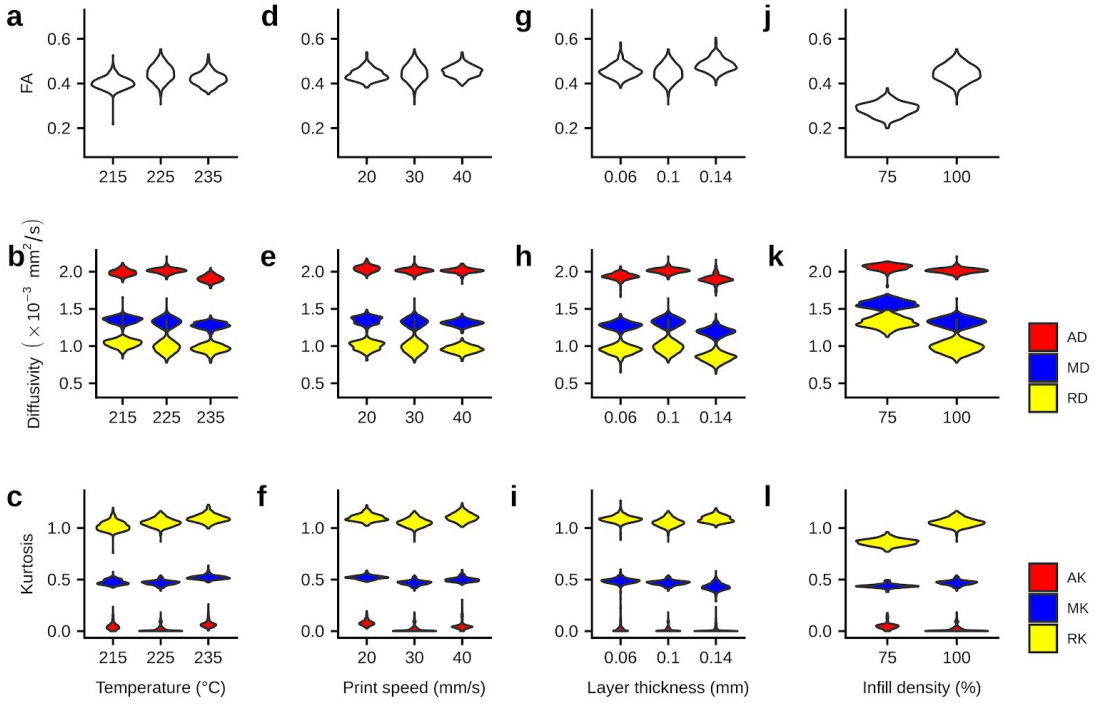

Figure 6. Mean FA, diffusivities, and kurtosis with different phantom printing parameters. a-c summarizes different metrics with different printing temperatures. d-f summarizes different metrics with different printing speeds. g-i summarizes different metrics with different layer thicknesses. j-l summarizes different metrics with different infill densities. Error bars at each point correspond to the standard deviation of the measured dMRI metric over all voxels within the phantom.

3.5 Metric stability over time

Over the 76 days of study, only small differences in mean value were observed for all metrics (< 7%, except for AK due to some very small values of AK), as seen in Figure 7.

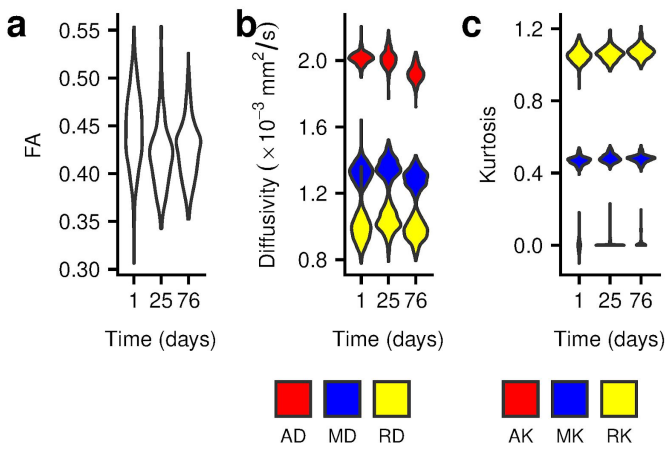

Figure 7. a) Mean Fractional anisotropy of a nominal phantom over 76 days. b) Mean Diffusivities of a nominal phantom over 76 days. c) Mean Kurtosis of a nominal phantom over 76 days. Error bars in all represent standard deviation of values in each corresponding phantom and scan time.

4. Discussion

4.1 Phantom vs. human microstructural fibre geometry

Microscopy images and synchrotron micro-CT images both indicate the presence of densely packed fibrous pores within a 3D printed composite material containing PVA within an elastomeric matrix. With typical diameters between 1.5-8 μm (Figure 3), these fibrous pores are larger than typical axons (17). However, the fibres are still narrow enough to modulate the diffusion signal at diffusion times typical for dMRI studies, so they can approximately mimic the anisotropic diffusion characteristics of axonal bundles. Notably, there may be smaller pores present that the confocal microscopy was unable to resolve which may have skewed the histogram to larger diameters. Nevertheless, the protocol introduced by this study produces long, straight pores that have a limited effect on diffusion along their path.

4.2 Phantom vs. human diffusion characteristics

The observed DKI metrics correspond well to those seen in real white matter but have some notable differences. The phantoms were scanned at room temperature, which has a lower diffusivity of free water (~0.0022 mm^2/s) than human body temperature (~0.003 mm^2/s) (18). This difference in the diffusivity of free water means that the diffusivity DKI metrics have a

higher maximum possible value in vivo, which should be accounted for when analyzing those metrics.

AD in the phantoms was close to the diffusivity of free water at room temperature, while coherently organized white matter in the brain typically has AD of about 0.001 mm^2/s, roughly a third of the diffusivity of free water at body temperature (19). This discrepancy indicates that the uniform fibre orientation and homogeneous microstructure of the phantoms results in a simpler axial diffusion environment than that observed in the brain. AK in the phantoms was close to zero, while practically all white matter regions in the brain have non-zero AK. This finding further supports the conclusion that there is an anatomically unrealistic homogeneity in the phantoms' microstructure; real tissue is more heterogeneous and structurally complex than the 3AM phantoms.

RD in the 3AM phantoms was much lower than the diffusivity of free water at room temperature, indicating that diffusion is hindered and/or restricted perpendicular to the axis of the pores. The mean RK in the nominal 3AM phantom is non-zero but lower than typical values in orientationally coherent white matter tracts (20). This indicates that the fibrous pores of the 3AM phantom restrict diffusion but do not recreate the structural heterogeneity of real white matter.

MD in the 3AM phantoms was about 63% of the diffusivity of free water at room temperature, while MD in real white matter is typically less than 33% of the diffusivity of water at body temperature. Partially due to the near-total lack of restriction or hindering of diffusion in the axial direction, there is less restriction/hindering of diffusion overall in 3AM phantoms than in white matter. MK in the 3AM phantoms was about half the typical values in human white matter (20), further indicating that 3AM phantoms have less heterogeneous microstructure than real axonal tracts.

The FA is within the range of typical values observed in the human white matter (19), but lower than that observed in the most coherent regions like the corpus callosum (21). The micro-CT images show gaps between adjacent lines of material even at 100% infill density, which leads to a non-negligible free water compartment within the phantoms. This free water compartment reduces the overall FA due to partial voluming, which suggests that a higher FA may be achievable with an altered 3D printing process. This free-water compartment

likely also contributes to the relatively low kurtosis values and the diffusivities being relatively close to the free water value.

4.3 Phantom reproducibility and stability

Infill density was the only print parameter that had a large effect on any of the DKI metrics, with its greatest effect on FA, RD, and RK. The likely explanation for this effect is that a lower infill density replaces the elastomeric matrix with free water, increasing the effect of partial voluming between the two components.

The small effect of the other 3D print parameters on the observed DKI metrics suggests that minor variations in print parameters across different 3D printers should not greatly affect the characteristics of the phantoms they print. However, this also means that it is likely not possible to change print parameters to tune a phantom's diffusion characteristics. That said, it may be possible to tailor diffusion characteristics using different porous filament materials. The low coefficient of variation across identical phantoms supports the conclusion that the 3AM phantom production protocol is repeatable, at least across multiple prints on a single printer with the same material.

The stability analysis showed only small changes over the time period of 2.5 months. This demonstrated stability of the phantom microstructure over a relatively long time period suggests that one prepared phantom sample can at least be transported to multiple sites in multi-centre studies without concern for parameter changes between scans.

4.4 Method advantages

The phantoms we have introduced are produced with FDM 3D printing, a widely accessible and inexpensive production technique. A single spool of printing material (~ $50 USD) can be used to produce hundreds of phantoms. The development of this technique lowers the barrier to entry for researchers to conduct phantom studies for validation of certain dMRI models of white matter. Such studies bridge the gap between simulations and studies using fixed tissue, serving as a useful option for the dMRI modeling community.

The three analyses performed for this study show the existence of axon-mimetic fibrous pores in 3AM phantoms that modulate dMRI signal to approximate white matter anatomy. By

analyzing the microstructure of the phantoms with both confocal microscopy and phase contrast micro-CT, we have confirmed that the fibrous pores in our phantoms are of an appropriate size and shape to mimic axonal fibres. These findings are supported by the observation of non-zero FA and RK. Furthermore, the quantitative T_1 and T_2 scans indicate that the phantoms do not shorten relaxation times enough to significantly reduce SNR in dMRI scans, and they can be reduced via doping (e.g., copper II sulphate) to better agree with values found in tissue.

FDM offers the flexibility to alter the print-head direction between layers, which may enable the exploration of crossing fibre effects and their associated models. In our preliminary investigations, FA reductions are observed with increasing fibre crossing angle. Future work will investigate optimal phantom design for validation of crossing fibre models.

5 Conclusion

In this study we introduce 3AM phantoms, a novel class of dMRI phantoms that are customizable, affordable, and straight-forward to produce. 3AM phantoms mimic the microporous structure of axon bundles in white matter, and the utilization of 3D printing likely opens the door for customizability and the production of complex, anatomically accurate phantoms.

Acknowledgements

This work was supported by the Canada First Research Excellence Fund, Brain Canada, and Discovery Grants from the Natural Sciences and Engineering Research Council (NSERC). Part of the research described in this paper was conducted at the BioMedical Imaging and Therapy (BMIT) facility at the Canadian Light Source Inc. (CLSI), which is funded by the Canada Foundation for Innovation, the Natural Sciences and Engineering Research Council of Canada, the National Research Council Canada, the Canadian Institutes of Health Research, the Government of Saskatchewan, Western Economic Diversification Canada, and the University of Saskatchewan.

References

1. Steven AJ, Zhuo J, Melhem ER. Diffusion kurtosis imaging: an emerging technique for evaluating the microstructural environment of the brain. AJR Am. J. Roentgenol.

2014;202:W26–33.

2. Beltrachini L, Taylor ZA, Frangi AF. A parametric finite element solution of the generalised Bloch-Torrey equation for arbitrary domains. J. Magn. Reson. 2015;259:126–134.

3. Grebenkov DS. Exploring diffusion across permeable barriers at high gradients. II. Localization regime. J. Magn. Reson. 2014;248:164–176.

4. Seehaus A, Roebroeck A, Bastiani M, et al. Histological validation of high-resolution DTI in human post mortem tissue. Front. Neuroanat. 2015;9:98.

5. Leergaard TB, White NS, de Crespigny A, et al. Quantitative histological validation of diffusion MRI fiber orientation distributions in the rat brain. PLoS One 2010;5:e8595.

6. Rokem A, Yeatman JD, Pestilli F, et al. Evaluating the accuracy of diffusion MRI models in white matter. PLoS One 2015;10:e0123272.

7. Benjamini D, Komlosh ME, Basser PJ, Nevo U. Nonparametric pore size distribution using d-PFG: comparison to s-PFG and migration to MRI. J. Magn. Reson. 2014;246:36–45.

8. Fan Q, Nummenmaa A, Wichtmann B, et al. Validation of diffusion MRI estimates of compartment size and volume fraction in a biomimetic brain phantom using a human MRI scanner with 300 mT/m maximum gradient strength. Neuroimage 2018;182:469–478.

9. Schilling KG, Gao Y, Stepniewska I, Janve V, Landman BA, Anderson AW. Histologically derived fiber response functions for diffusion MRI vary across white matter fibers - an ex vivo validation study in the squirrel monkey brain. bioRxiv 2018:438978 doi: 10.1101/438978.

10. Yanasak N, Allison J. Use of capillaries in the construction of an MRI phantom for the assessment of diffusion tensor imaging: demonstration of performance. Magn. Reson. Imaging 2006;24:1349–1361.

11. Hubbard PL, Zhou F-L, Eichhorn SJ, Parker GJM. Biomimetic phantom for the validation of diffusion magnetic resonance imaging. Magn. Reson. Med. 2015;73:299–305.

12. Abu-Sardanah SO, Hussain U, Moore J, Baron C, Peters T, Khan AR. Design and evaluation of a diffusion MRI fibre phantom using 3D printing. In: Medical Imaging 2018: Physics of Medical Imaging. Vol. 10573. International Society for Optics and Photonics; 2018. p. 105731Q.

13. Mushtaha FN, Kuehn TK, Moore J, Khan AR, and Baron CA. Microstructural characterization and validation of a 3D printed phantom for diffusion MRI. In Proceedings of the 27th Annual Meeting of ISMRM, Montreal, Canada, 2019. 0649.

14. Fieremans E, Lee H-H. Physical and numerical phantoms for the validation of brain microstructural MRI: A cookbook. Neuroimage 2018;182:39–61.

15. Bradley D, Roth G. Adaptive Thresholding using the Integral Image. Journal of Graphics Tools 2007;12:13–21.

16. Garyfallidis E, Brett M, Amirbekian B, et al. Dipy, a library for the analysis of diffusion MRI data. Front. Neuroinform. 2014;8:8.

17. Liewald D, Miller R, Logothetis N, Wagner H-J, Schüz A. Distribution of axon diameters in cortical white matter: an electron-microscopic study on three human brains and a macaque. Biol. Cybern. 2014;108:541–557.

18. Mills R. Self-diffusion in normal and heavy water in the range 1-45.deg. J. Phys. Chem. 1973;77:685–688.

19. Alexander AL, Lee JE, Lazar M, Field AS. Diffusion tensor imaging of the brain. Neurotherapeutics 2007;4:316–329.

20. Jensen JH, Falangola MF, Hu C, et al. Preliminary observations of increased diffusional kurtosis in human brain following recent cerebral infarction. NMR Biomed. 2011;24:452–457.

21. Ciccarelli O, Werring DJ, Barker GJ, et al. A study of the mechanisms of normal-appearing white matter damage in multiple sclerosis using diffusion tensor imaging--evidence of Wallerian degeneration. J. Neurol. 2003;250:287–292.